

Impact of Inland Terrain on Mid-Atlantic Offshore Wind and Implications for Wind Resource Assessment: A Case Study

EDWARD STROBACH

University of Maryland, Baltimore County, Baltimore, Maryland

LYNN C. SPARLING

University of Maryland, Baltimore County, and Joint Center for Earth Systems Technology, Baltimore, Maryland

SCOTT DANIEL RABENHORST

National Research Council/Naval Research Laboratory, Washington, D.C.

BELAY DEMOZ

University of Maryland, Baltimore County, and Joint Center for Earth Systems Technology, Baltimore County, Baltimore, Maryland

(Manuscript received 26 May 2017, in final form 21 December 2017)

ABSTRACT

This paper presents a case study of a strong low-level jet (LLJ) that was observed about 20 km off the coast of Ocean City, Maryland, during a measurement campaign in the summer of 2013. Doppler wind lidar observations offshore, together with analyses of 4-km WRF Model data and NARR data, are used to reconstruct the forcing mechanisms that led to the growth and rapid collapse of the jet offshore as well as to differentiate the forcing mechanisms resulting in an LLJ farther inland. It was observed that the LLJ over the mid-Atlantic coastal plain decreased gradually throughout the early morning hours relative to the LLJ along the coastal ocean as a downslope wind moved eastward from the Appalachian Mountains. The forcing of the LLJ was a result of both thermal and mechanical mechanisms linked to the topography, while synoptic forcing from an approaching cold front led to a downslope wind. Data from a wind profiler near Cambridge, Maryland, also showed an LLJ, but forced by different regional conditions, emphasizing the difficulties of inferring wind conditions offshore from onshore observations. The sudden breakdown of the jet offshore appears to have been a result of an interaction with a downslope wind from the Appalachian Mountains. This particular case study highlights the 1) importance of both large-scale and regional forcing, 2) impact that topographical forcing farther inland had on offshore wind, and 3) different responses in the wind profile as a downslope wind moved across the mid-Atlantic region.

1. Introduction

The development of coastal and offshore wind energy is moving forward as one of several options for greener solutions to the problem of energy generation along the populous U.S. East Coast (Beaudry-Losique et al. 2011). Unlike offshore wind development in Europe, one of the challenges for wind resource assessment along the

U.S. East Coast is the lack of long-term records of marine boundary layer winds and thermal stability at turbine hub height and across the rotor span. The need for more offshore observations along the East Coast is widely recognized (e.g., Archer et al. 2014), and some recent measurement campaigns have begun to address this issue (e.g., Sparling et al. 2013; Colle et al. 2016). In regions where there is no long-term record of hub-height winds (i.e., winds between 60 and 120 m for the smallest and largest turbines in current operation, respectively), measurement campaigns—although limited in scope—can nevertheless be used together with model simulations to gain some insight into regional wind forcing mechanisms that may not be represented in

 Denotes content that is immediately available upon publication as open access.

Corresponding author: Edward Strobach, estrob1@umbc.edu

DOI: 10.1175/JAMC-D-17-0143.1

© 2018 American Meteorological Society. For information regarding reuse of this content and general copyright information, consult the [AMS Copyright Policy](https://www.ametsoc.org/PUBSReuseLicenses) (www.ametsoc.org/PUBSReuseLicenses).

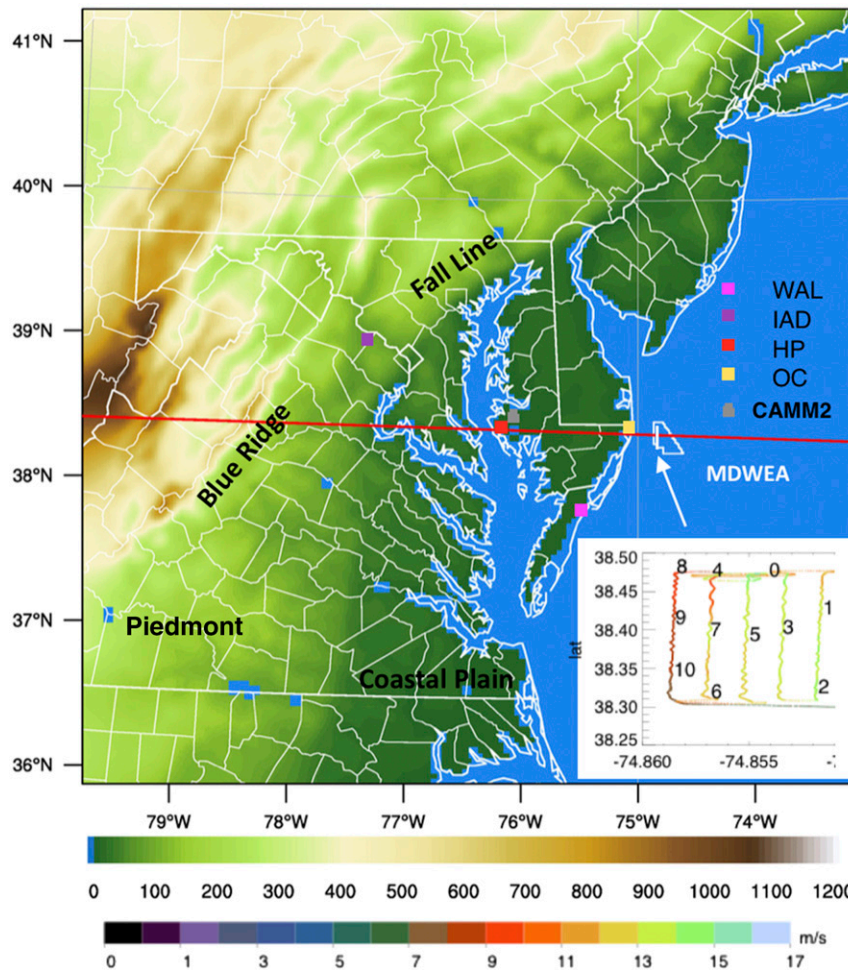


FIG. 1. A geographical map of the southern mid-Atlantic region highlighting the Blue Ridge Mountains, Piedmont Plateau, the coastal plain, and the fall line. Observational sites and platforms are designated by the colored squares and show the locations of the Sterling sounding launch site (purple square), HP laboratory (red square), the National Buoy Data Center (NBDC) buoy at Cambridge (CAMM2; gray square), the NBDC buoy at Ocean City (OCIM2; yellow square), and Wallops Island sounding launch site (pink square). MDWEA (white bordered area east of the Delmarva coast) shows the ship track during the case study with an inset of 100-m winds along the track path with time in UTC. A horizontal red line is also provided as the transect analyzed and presented in the study.

low-resolution reanalysis climatologies (e.g., Cuxart et al. 2000; Poulos et al. 2002).

The focus of this study is in the mid-Atlantic region where there are few offshore observations, and where the variability of the terrain can lead to complex low-level wind regimes both on- and offshore. Surface features such as the Appalachian Mountains, the Chesapeake and Delaware Bays, and the morphology of the coastline result in mesoscale phenomena such as low-level jets (LLJs), downslope winds, and sea-land breezes and bay breezes. Other geographical features include the Appalachian deformation boundary across southern Pennsylvania and the fall line, the boundary between the coastal plain and

Piedmont, which extends about 900 mi (1450 km) along the coast. The physiography of the region considered in this paper, illustrated in Fig. 1, has local and regional features that can result in complex multilayered wind speed and wind direction profiles, especially during the warm season when synoptic forcing is weak. This can lead to substantial changes in wind speed within a short period of time, as shown by the inset diagram of the 100-m wind speed. To determine the cause of these changes, a combination of model data and observations (denoted by squares in Fig. 1) must be included in the analysis.

On larger scales, the Bermuda high to the southeast leads to prevailing southwesterly winds with the

potential for coastal upwelling in the Mid-Atlantic Bight (MAB; Schofield et al. 2008) that can lower the sea surface temperature (SST) and increase the baroclinicity of the lower atmosphere along the coast. The combination of southwesterly winds and enhanced baroclinicity can promote the generation of shallow coastal LLJs with substantial wind shear. An example where coastal LLJs have been observed frequently is along the New York Bight (NYB) that extends from northern New Jersey to Long Island, New York (Colle and Novak 2010). In the study conducted by Colle and Novak (2010), it was found that the NYB jet occurred most often during the summer months and that the jet coincided with strong cross-coastal temperature gradients. This is significantly different than the coastal plain LLJ in that the coastal plain LLJ is a nocturnal phenomenon that tends to result from either a significant reduction of friction during day-to-night transitions (i.e., acceleration and destabilization of wind leading to inertial oscillation pattern) or cross-mountain baroclinicity (Ryan 2004; Zhang et al. 2006).

The Appalachian Mountains have also been known to significantly impact boundary layer winds in the mid-Atlantic region (Gaffin 2002; Decker and Robinson 2011) and lead to downslope winds, severe weather, or cold-air damming (Bell and Bosart 1988; Decker and Robinson 2011; Rabenhorst et al. 2014). A recent study by Rabenhorst et al. (2014) found that a downslope wind descending from the Appalachian Mountains can result in a subtle, yet complex interaction between winds aloft (descending downslope wind) with winds near the surface.

Similar evolutionary characteristics in the wind profile observed by Rabenhorst et al. (2014) were noted throughout a 6-week period (19 June–31 August) during the summer of 2013, with the Maryland Wind Energy Area (MDWEA; white polygon in Fig. 1) serving as a test bed for profile measurements of marine boundary layer winds. The day chosen for this case study, 19 July 2013, revealed the development of an LLJ over the coastal plain region and along the east coasts of Delaware, Maryland, and Virginia (Delmarva) early in the evening (0100–0330 UTC, coastal plain; 0100–0630 UTC, MDWEA). The data gathered offshore came from a Doppler wind lidar instrument and provided the first comprehensive set of measurements of marine boundary layer wind profiles in this area. During the measurement campaign, strong winds ($>8 \text{ m s}^{-1}$) lasting at least 2 h were observed roughly 30% of the time at a height of 100 m during days where data availability was 3 h or more (51 days total). This particular case study was chosen primarily to illustrate the 1) importance of both large-scale and regional forcing, 2) impact that

topographical forcing farther inland had on offshore wind, and 3) different responses in the wind profile as a downslope wind moved across the mid-Atlantic region. In addition, since both LLJs and a downslope wind were observed during this study and are common to this region, it is important to better understand this interaction in order to forecast potential “ramp-down events,” or instances in which winds substantially decrease over a short period of time.

The remainder of this paper is organized as follows. Section 2 is a brief overview of the mechanisms that force the LLJ and downslope wind, with emphasis on the mid-Atlantic region, and section 3 discusses the data and methodology used. Section 4 presents the case study with a multiscale analysis that includes model data from the Weather Research and Forecasting (WRF) Model, reanalysis data from the North America Regional Reanalysis (NARR), and observational data from both the Doppler wind lidar offshore and a radar wind profiler onshore. Section 5 is a summary of the main results, conclusions, and implications for wind resource assessment and prediction.

2. Background

a. Low-level jet

A low-level jet is a mesoscale maximum in the wind profile at heights between 100 and 1000 m AGL. LLJs can occur frequently at night (i.e., nocturnal LLJs) over land, are narrow in width, and can extend for hundreds of kilometers along the direction of the wind. Specific criteria used to identify LLJs have been used to develop regional climatologies, for example in the Great Plains (e.g., Bonner 1968; Whiteman et al. 1997), all of which emphasize strong wind shear above and below the jet. Like nocturnal LLJs, coastal LLJs exhibit a similar wind profile structure but can occur during the day or night depending on both the cross-coastal surface temperature gradient and background conditions (Colle and Novak 2010).

Several well-known mechanisms are attributed to LLJ formation. Blackadar's inertial oscillation theory (Blackadar 1957) explains the formation of LLJs as a result of nighttime radiative cooling at the surface, which reduces the turbulent stresses and allows the winds to accelerate under constant geostrophic forcing. Pure inertial oscillations are not common, however, and departures from the ideal case can sometimes be used to identify additional forcing mechanisms (e.g., Van de Wiel et al. 2010; Shapiro et al. 2016). Van de Wiel et al. (2010) developed a model that includes boundary layer drag by defining the inertial rotation with respect to an “equilibrium” wind at each vertical level to take into

account the Ekman rotation of wind with height in the boundary layer and found good agreement with observations.

Another LLJ forcing mechanism is large-scale baroclinicity over sloping terrain. Holton (1967) proposed that the horizontal temperature gradient at a constant height level near the ground reverses direction at night as a result of radiational cooling, with little change in the temperature gradient aloft. Using a thermal wind argument, this gives rise to a baroclinic zone and a wind maximum between the two levels. This mechanism is important for the formation of the mid-Atlantic coastal plain LLJ, which is not uncommon during the warm season and occurs under clear conditions that promote strong cooling of the elevated terrain to the west (Ryan 2004; Zhang et al. 2006). Shapiro et al. (2016) developed a model that combined the inertial oscillation and sloping terrain mechanisms and found good agreement with observations.

LLJs that form along the coast as a result of cross-coastal baroclinicity are important for offshore wind energy and have been observed in the New York Bight and other locations in the Northeast (Mahrt et al. 2014; Colle et al. 2016). Significant differences exist between coastal jets along the East Coast and the California barrier jet where westerly flow is blocked by coastal orography (Burk and Thompson 1996). The orographic influence along the west coast can also extend far offshore (Holt 1996). An investigation of the Carolina coastal LLJ showed the importance of baroclinicity associated with large-scale sloping terrain and the land-sea boundary as important forcing elements (Doyle and Warner 1993). A recent study examined the development of LLJs off the coast of New Jersey (Nunalee and Basu 2014) and found that coastal LLJs in this region were due primarily to shallow baroclinic zones from land-sea temperature differences, rapid radiational cooling at night over land, and cooler SSTs where coastal upwelling is evident.

Other factors that can lead to or strengthen a preexisting LLJ include the advection of an internal boundary layer and the acceleration of winds across coastal or roughness boundaries, as shown in the study by Barthelmie et al. (2007) evaluating winds crossing over into the Baltic Sea. The height and strength of LLJs depend on the orientation of winds with respect to the boundary and horizontal gradients in stability as the winds cross the boundary. Spatial variability near coastal regions is due to the fact that sensible heat flux from the land surface is more variable than over water (Muñoz et al. 2008) and the morphology of the coastline (Baker et al. 2001).

The combination of different forcing mechanisms as described above, along with the influence of the

large-scale conditions, can play a significant role in the evolution of the LLJ as discussed in recent studies (e.g., Van de Wiel et al. 2010; Nunalee and Basu 2014; Shapiro et al. 2016).

b. Downslope wind

The impact of topography on winds, and the subsequent generation of a downslope wind in the lee of the mountains, depends on the thermal stability across the mountain (Durran 2003; Meyers et al. 2003; Seluchi et al. 2003), wind shear over the mountains (Ralph et al. 1997; Monti et al. 2002; Meyers et al. 2003), and the internal variability of the topography (Reinecke and Durran 2008; Zardi and Whiteman 2013). A combination of synoptic conditions, variations in sensible heat fluxes over terrain, an evaluation of upstream flows blocked by the mountains, and the Scorer parameter is often used to assess the likelihood of a downslope wind in the lee of the mountains (Smith 1976; Banta and Gannon 1995; Gaffin 2002; Schultz and Trapp 2003; Houze 2012).

In general, downslope winds can occur anywhere where there is rolling terrain. Characteristics of the downslope wind, which include horizontal variability, intensity, and the shape of the wind profile depend on such factors as the background conditions, the angle of the slope, and the internal roughness of the terrain (Whiteman and Doran 1993; Haiden and Whiteman 2005; Whiteman and Zhong 2008; Zardi and Whiteman 2013).

It is important to note, however, that the term “downslope wind” is different from a katabatic wind, which is a wind generated as the sloping terrain undergoes significant radiative cooling (Durran 2003). Depending on wind speed and thermal stability, a downslope wind can result in the formation of a gravity current or undular bore, in which denser air displaces warm air on the lee side (Grachev et al. 2016). The change in temperature across the mountains during a downslope wind event is a result of cooling at the summit from adiabatic expansion and warming at the foothills due to adiabatic compression (Zardi and Whiteman 2013).

In some cases, the formation of a downslope wind is a result of a frontal system approaching the windward side of the mountains (Schultz 2005; Thompson 2012; Rabenhorst et al. 2014), which is important for this case study. A typical indication that a downslope wind is forming is by assessing whether the rotation of winds can be linked to significant deepening of the lee trough.

Much of the research regarding downslope winds in the United States has focused on the eastern slopes of the Rocky Mountains. Numerous theoretical studies (e.g., Peng et al. 1995; Durran 2003; Seluchi et al. 2003; Huang et al. 2010), as well as analyses of data from

simulations and observations, find that downslope winds also occur in the presence of modest terrain. A multiyear statistical study by Thompson (2012) noted the presence of the Appalachian lee trough 26.6% of the time during the warm season, suggesting that the generation of downslope winds may occur frequently in the lee of the Appalachian Mountains. Moreover, the combined likelihood of downslope wind generation with other frequently observed low-level sheared flows such as LLJs suggests possible complex interactions between wind regimes that may result in these so-called ramp-down events. This study intends to examine the development of the downslope wind, the link between the downslope wind and the lee trough, and the features of the inland terrain that allowed the downslope wind to propagate offshore and interact with boundary layer wind profiles both on- and offshore.

3. Data and methods

Marine boundary layer winds were measured using the Offshore V2 WindCube (Leosphere). The WindCube measured winds in the vertical range (40–220 m) at 20-m vertical resolution. A lidar was mounted on a ship during a geophysical survey of the seafloor in the MDWEA, and data were gathered while the ship was under way at about 3 m s^{-1} . The survey tracks generally followed a north–south path with occasional turnaround points that were filtered from the analysis. The insert in Fig. 1 depicts the path of the ship during the period of this study, with the 100-m wind speed from the lidar indicated in color. North–south tracks were separated by only 150 m, so the times marked on the ship track show several instances where the ship was nearly in the same location. Both motion-compensated and raw (uncompensated) data were available at a high temporal resolution ($\sim 1 \text{ s}$). Corrections for roll, pitch, and yaw were made by the instrument's motion compensation algorithm using a time-synched inertial navigational unit (INU). It was found that the motion rarely exceeded a 1° tilt; translational motion was independently corrected using a differential GPS. Lidar data availability was limited to the evening hours (0030–1100 UTC, 2030–0700 LT) since the instrument experienced issues with overheating during the day.

A 915-MHz radar wind profiler at the Horn Point (HP) Laboratory in Cambridge, Maryland, provided onshore wind profile data. Of the several regional wind profilers available, HP was closest to the MDWEA. The profiler operated with a temporal resolution of 6 min and a vertical resolution of 60 m. The base measurement of the profiler was 152 m above sea level, with measurements of the wind occasionally exceeding 4 km.

Since low signal to noise was a factor at higher heights, the wind retrieval was often limited to 2.5 km. HP data were used to compare onshore and offshore wind profiles and assess the regional extent of the LLJ, to quantify contributions from the downslope wind, and to investigate differences at low levels due to local regional forcing. A nearby buoy station was used for near-surface ($\sim 5 \text{ m}$ above sea level) wind observations. The buoy anemometer reported wind speeds every 6 min at a time stamp matching the radar wind profiler. Winds at two additional levels between 5 and 152 m were approximated by linear interpolation. Linear interpolation was chosen over logarithmic interpolation for several reasons. 1) The stable boundary layer height, which in the presence of an LLJ is often correlated with the height of the jet maximum (Banta et al. 2006), was near the 150-m level for both observations and the WRF Model; 2) the similarity theory has been found to break down for stable regimes, thus rendering the logarithmic wind profile a poor assumption (Mahrt 1998); 3) the surface layer only represents 10% of the boundary layer (i.e., 15 m); and 4) a near-linear wind shear profile is most often observed below the wind maximum of an LLJ (Banta 2008).

Other nearby sources of data, including National Data Buoy Center buoys and National Weather Service (NWS) Automated Surface Observing System stations at Sterling, Virginia (IAD), and Wallops Island, Virginia (WAL), were used to evaluate conditions at different locations across the mid-Atlantic region. Unfortunately, no offshore thermal profiles were available for this study; the closest thermal profile to MDWEA was the Wallops Island radiosonde, located to the southwest of the survey area. The locations of data sources used in this study are shown in Fig. 1.

A high-resolution (4 km) simulation was performed with the version 3.5 of the WRF Model (Skamarock and Klemp 2008); the boundary of the high-resolution domain extends from northern Pennsylvania to northern North Carolina, and extends from the Appalachian ridgeline to the coastal ocean. The Mellor–Yamada–Janjić (MYJ) planetary boundary layer scheme (Janjić 1994) was used and WRF physics options included the Noah land surface model (Chen and Dudhia 2001), the RRTM radiative transfer model (Iacono et al. 1998), Goddard microphysics, and the Urban Canopy Model. No cumulus parameterizations were used for these runs. The 2-h forecasts from the 0000, 0100, 0200, . . . , 2300 UTC cycles of the Rapid Refresh for input were used as initial and boundary conditions; for example, the boundary conditions at 1200 UTC used the 1000 UTC RAP analysis cycle with a forecast valid at 1200 UTC. Overall fields (especially wind) were closer to our

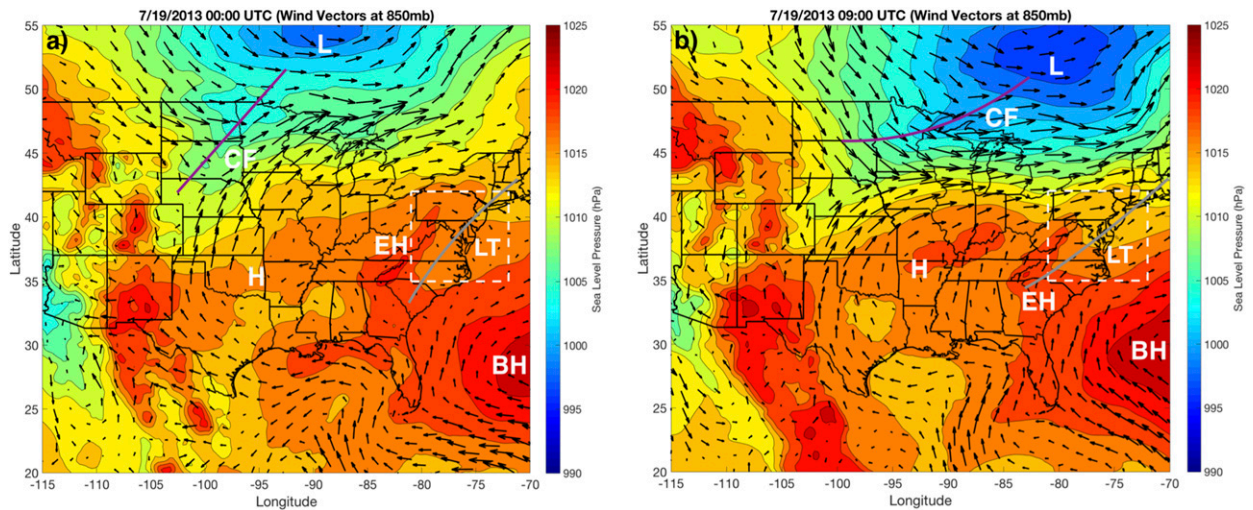


FIG. 2. The 850-hPa winds (vectors) and sea level pressure (colors) across much of the United States at (a) 0000 and (b) 0900 UTC from NARR. Annotations are included to point out meteorological features from NOAA surface analyses such as high pressure systems (BH, Bermuda high; EH, eastern high; H, high), low pressure systems (L), the Appalachian lee trough (LT; gray line), and a cold front (CF; solid purple line). The white dashed lines denote the area of focus for our study of mesoscale features and approximates the size of the WRF domain.

observations with 2-h forecasts. Nudging options were also available and issued every analysis cycle to ensure an accurate regional forecast. Vertical (σ) levels were spaced every 15 m up to 200 m, with 30 σ levels below 700 m, and vertical resolution at 2400 m and above was 200 m or greater. The advantage of lower grid spacing near the surface enabled the characterization of stable boundary layer flows in the presence of terrain as well as offering a comparison with observations. WRF was used to characterize the observations in terms of the regional variability of the wind and thermal stability from the Appalachian Mountains to MDWEA, and to understand how orographic forcing may have contributed to observations offshore.

The NARR dataset was used to evaluate the synoptic conditions across the mid-Atlantic region. The NARR data are accessible online (<http://www.esrl.noaa.gov/psd/data/gridded/data.arr.html>) every 3 h at pressure levels separated by 50 hPa (1000, 950, 900 hPa, ...). NARR data were used to determine the synoptic-scale drivers for the evolution of the mesoscale dynamics seen in the WRF simulations that in turn explained the variability on smaller regional scales in the observations.

4. Results

a. Synoptic overview

The goal of this section is to evaluate the large-scale forcing conditions that impacted the southern mid-Atlantic region. We show the NARR sea level pressure and 850-hPa (≈ 1.6 km MSL) winds on 19 July 2013

at 0000 UTC (Fig. 2a) and 0900 UTC (Fig. 2b). Earlier in the evening (0000 UTC), the large-scale conditions over the mid-Atlantic region were dominated by a high pressure system over the eastern portion of the United States (labeled as EH) and the Bermuda high offshore to the southeast (BH). Southwesterly winds are evident west of BH along the coast of the Carolinas at 0000 UTC (2000 LT), which when combined with northwesterly flows from EH and daytime convection led to a weak and complex flow pattern over the southern mid-Atlantic region. By 0900 UTC (0500 LT) winds shifted more toward the east over the southern mid-Atlantic region with winds maintaining a southwesterly flow farther offshore. The preservation of southwesterly flows farther east provided ideal background conditions for the LLJ since the overall forcing, both on the large scale and regionally, were in the same direction.

A trough located in the lee of the Appalachian Mountains (gray line in Fig. 2) is evident from the sea level pressure shown in Figs. 2a and 2b. The trough during the late afternoon was likely a vestigial remnant of a thermal low since the synoptic situation was weak along the East Coast at that time. As the synoptic situation changed and a low pressure system over Canada (L) moved eastward and deepened with time, winds began to rotate from southwesterly to westerly, thereby contributing to a deepening of the lee trough later in the evening. The deepening of L is demonstrated by the decreasing sea level pressure about the center and is likely related to possible frontogenetical forcing. Although frontogenesis was not investigated in detail, the

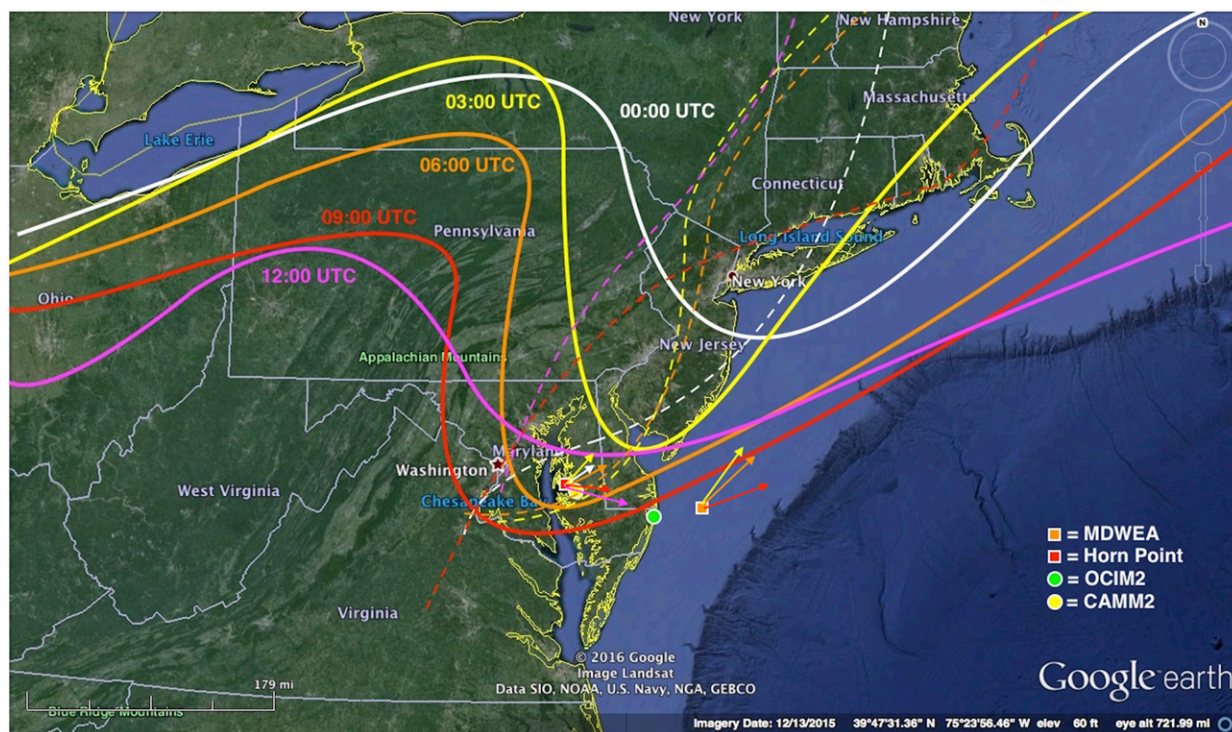


FIG. 3. The 1016-hPa pressure contours from NOAA WPC superimposed onto a Google Earth map and color-coded according to time. Additional symbols are included to show HP (red square), MDWEA (orange square), and various buoys (circles). The approximate axis of the trough is shown by color-coded dashed lines, while wind vectors at 200 m are superimposed on both sites, which are also color coded according to time.

distance between isobars extending from L decreased from 0000 to 0900 UTC, with winds south of L strengthening with time. The eastward progression of L also shows alignment with a high pressure system over the southern United States (H), which resulted in a north–south orientation of the pressure gradient and a rotation of winds from a southwesterly to westerly. This led to cross-mountain flows and a clear shift in the wind direction favoring westerlies over the mid-Atlantic region. Figure 3 shows the time progression of the lee trough every 3 h (0000–1200 UTC) using the 1016-hPa pressure isobar extracted from NOAA Weather Prediction Center (WPC) surface analysis. It is clearly shown that the lee trough deepened with time, which also correlates with wind vector rotation at Cambridge (red square in Fig. 3) and MDWEA (orange square in Fig. 3) at 200 m above ground level using the radar wind profiler and Doppler wind lidar, respectively.

b. Mesoscale overview

The formation of the downslope wind, which is associated with the deepening of a lee trough with time, is illustrated in Fig. 4. Between 0300 and 1200 UTC, the wind vectors (u , w) reveal flow up and over the

mountains along an east–west transect through MDWEA at 38.3°N (shown as a red line in Fig. 1). Beneath the stable layer inversion in Figs. 4c–e, the flows are blocked and forced to move along the axis of the mountains in a southwesterly direction and contribute to an enhanced pressure ridge to the windward side of the mountains. Above the stable layer, the flow moved across the mountaintop and descended downslope nearly perpendicular to the mountain axis from a northwesterly direction (i.e., path of least resistance). It is apparent that the thermal structure was modified by the descending winds as a result of adiabatic warming, as shown by the horizontal variations in potential temperature as the downslope wind moved into the coastal plain toward MDWEA (i.e., gray dashed line in Fig. 4) between 0300 and 1200 UTC in Figs. 4b–e. This contributed to both an enhanced stable boundary layer near the surface and a decrease in the overall stability above the inversion, a well-known mechanism for channeling wave energy and supporting the propagation of a downslope wind (Crook 1988). Moreover, significant changes in stability along the transect are evident in Figs. 4c–e (i.e., between 0600 and 1200 UTC), which shows the differences in the vertical structure of

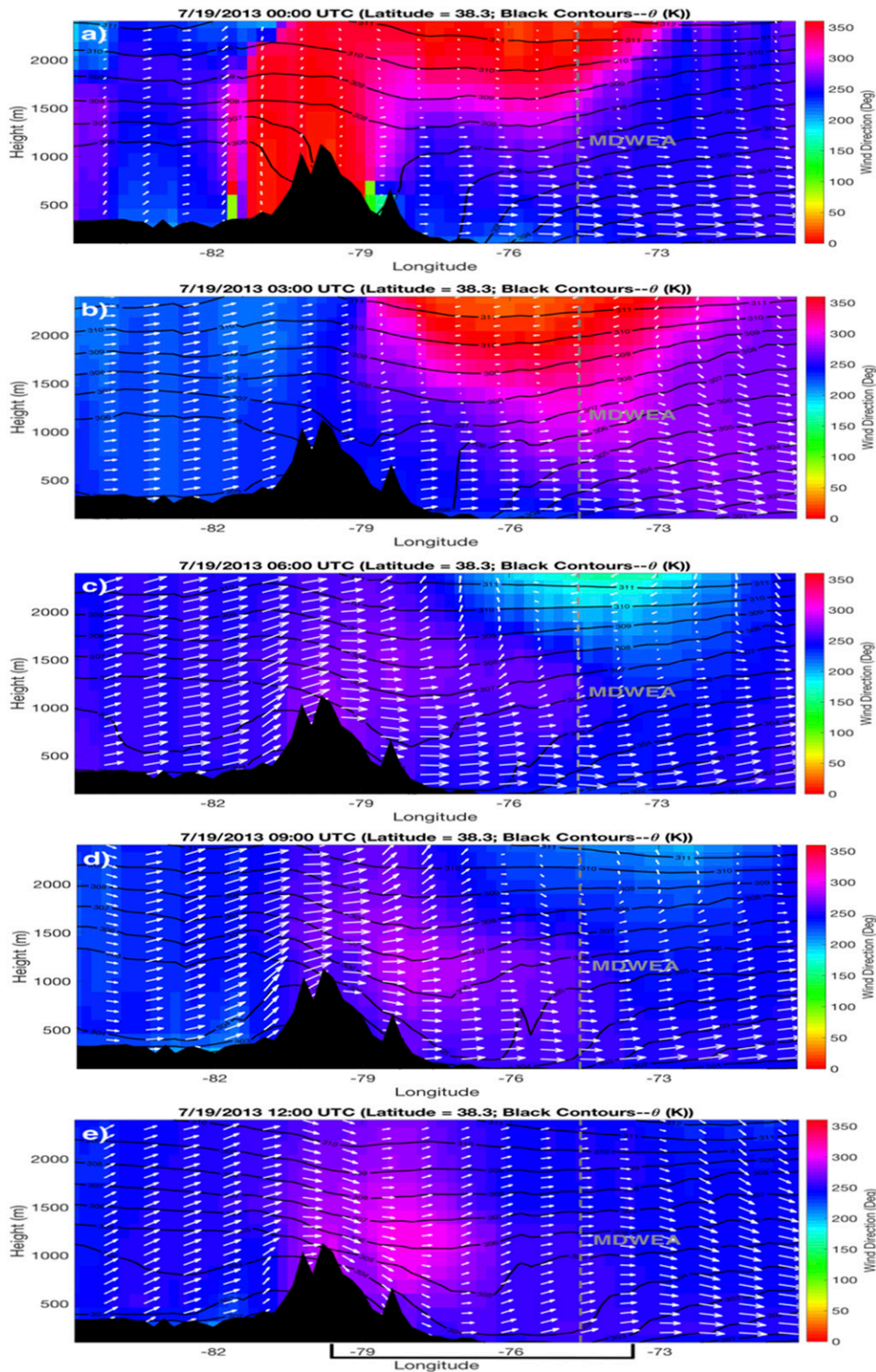


FIG. 4. Wind direction (colors), wind vectors (u , w ; white arrows), and potential temperature (black contours) from NARR at (a) 0000, (b) 0300, (c) 0600, (d) 0900, and (e) 1200 UTC along the east–west transect shown in Fig. 1. A vertical gray dashed line between -76° and -73° longitude is included to show the approximate position of MDWEA along the transect, while the black bracket at the bottom of the figure shows the east–west extent of the WRF domain and the longitudinal limit used in Fig. 8, below.

potential temperature across the terrain. The decreased stability in the lee of the mountains coincides with the location of the trough—higher absolute vorticity—while increased stability over the ridge coincides with the location of the pressure ridge—lower absolute vorticity.

Calculations of the Froude number [i.e., $U/(Nh)$] at different times, where U is the cross-mountain wind, N is the Brunt–Väisälä frequency above the stable layer inversion on the windward side (i.e., within the weakly stable residual layer), and h is the obstacle height as viewed from the windward side of the mountains (Durran 2003; Reinecke and Durran 2008; Mercer et al. 2008), also reveal the expected conditions for downslope winds between 0600 and 0900 UTC, with values of 1.16 and 1.20, respectively. Other times coincide with Froude numbers within the subcritical level (i.e., blocked flow), with values of 0.94 and 0.60 during 0300 and 1200 UTC, respectively. From Fig. 4, it is clear that weaker stability from the residual layer and increasing winds on the windward side by the mountains led to supercritical flow (i.e., unblocked flow) between 0600 and 0900 UTC. This led to what appeared to be a hydraulic-like jump observed in potential temperature on the leeside that coincides with northwesterly flows along the slope into the coastal plain shown in Figs. 4c and 4d and is a typical signature of a downslope wind. As stability increased on the windward side by 1200 UTC and winds weakened, the Froude number decreased and the lee trough became less pronounced, as noted earlier in Fig. 3.

c. Observations at HP and MDWEA and other regional observations

Figure 5 shows the northward wind component, v (black contours), and eastward wind component, u (colors), with moderate-to-strong low-level wind maxima at HP (radar wind profiler) and MDWEA (Doppler wind lidar) during the early morning hours of 19 July. Winds over HP at 0000 UTC (Fig. 5a) were from the south to southwest near 200 m AGL and increased with time to a maximum by 0330 UTC. This is coincident with the beginning of a second wind maximum in the westerly wind, which is defined by a simultaneous decrease (increase) in v (u) delineated by a solid gray line in Fig. 5a. The u -wind speed maximum is stronger ($\sim 14 \text{ m s}^{-1}$) and occurs at a higher altitude ($\sim 400 \text{ m}$) relative to the v -wind maximum of 7 m s^{-1} near 200 m, which translates to a wind speed maximum of 10 m s^{-1} given the orientation of the actual wind vector (i.e., approximately from the southwest). The maximum wind speed at the jet core near 400 m occurs around 0700 UTC, and maintains a westerly-to-northwesterly flow. By 1100 UTC the westerly wind maximum weakened to 8 m s^{-1} .

Around 0000 UTC (sunset) winds from the lidar increased with time from the south-southwest (210° – 220°). A coastal LLJ developed shortly after sunset [i.e., around 0100 UTC (0900 LT)], which strengthened from 9 to 13 m s^{-1} and increased in height from 80 to 200 m until 0500 UTC. Despite the height limitations of the lidar, it is clear that the LLJ decreased as eastward winds increased from aloft, shown schematically by the black arrow in Fig. 5b and an abrupt decrease in winds that occurred between 0630 and 0715 UTC.

To better demonstrate the similarities and differences between HP and MDWEA, winds were averaged between the lower limit of the HP profiler at 150 m and the upper limit of the lidar at 220 m; a comparison of the u and v components is shown in Fig. 5c. In both cases, the southerly wind increases with time (0000–0300 UTC), levels off, then declines significantly. During the observed change in v , the westerly wind component increased until 0700 UTC. The rates of change observed in u are almost identical with time for both sites, suggesting that both sites experienced similar forcing from the west that contributed to enhanced westerly flows. The response in the northward wind component between sites, however, varied in that winds exhibited a subtler decrease at HP that began around 0330 UTC, while winds at MDWEA maintained a nearly consistent magnitude for several hours until decreasing suddenly around 0700 UTC.

Additional observations from nearby NWS stations at Sterling and Wallops Island are also included to evaluate the extent of the downslope wind (Figs. 6a,b). In both cases, a clear westerly wind maximum was observed, with maximum winds of about 9 and 5 m s^{-1} at 350 m for Wallops Island and Sterling, respectively, at 1200 UTC. Moreover, the low-level wind shear between MDWEA and Wallops Island was found to be almost identical, which indicates that the overall wind conditions and forcing from the west were similar across a broader region from Virginia and Maryland. As observed in both radiosondes, the low-level stability was very strong, with the wind maximum between 50 and 100 m above the inversion.

d. Regional forcing mechanisms

In this section, the local forcing of the onshore and offshore LLJs using WRF is considered in order to understand the differences between them and to ascertain what features of the offshore LLJ can be inferred from measurements onshore. The emphasis here is on the inertial oscillation, the development of low-level baroclinicity, and internal boundary layer advection across terrain discontinuities. In addition, the evolution of the forcing conditions is considered for both sites in order to

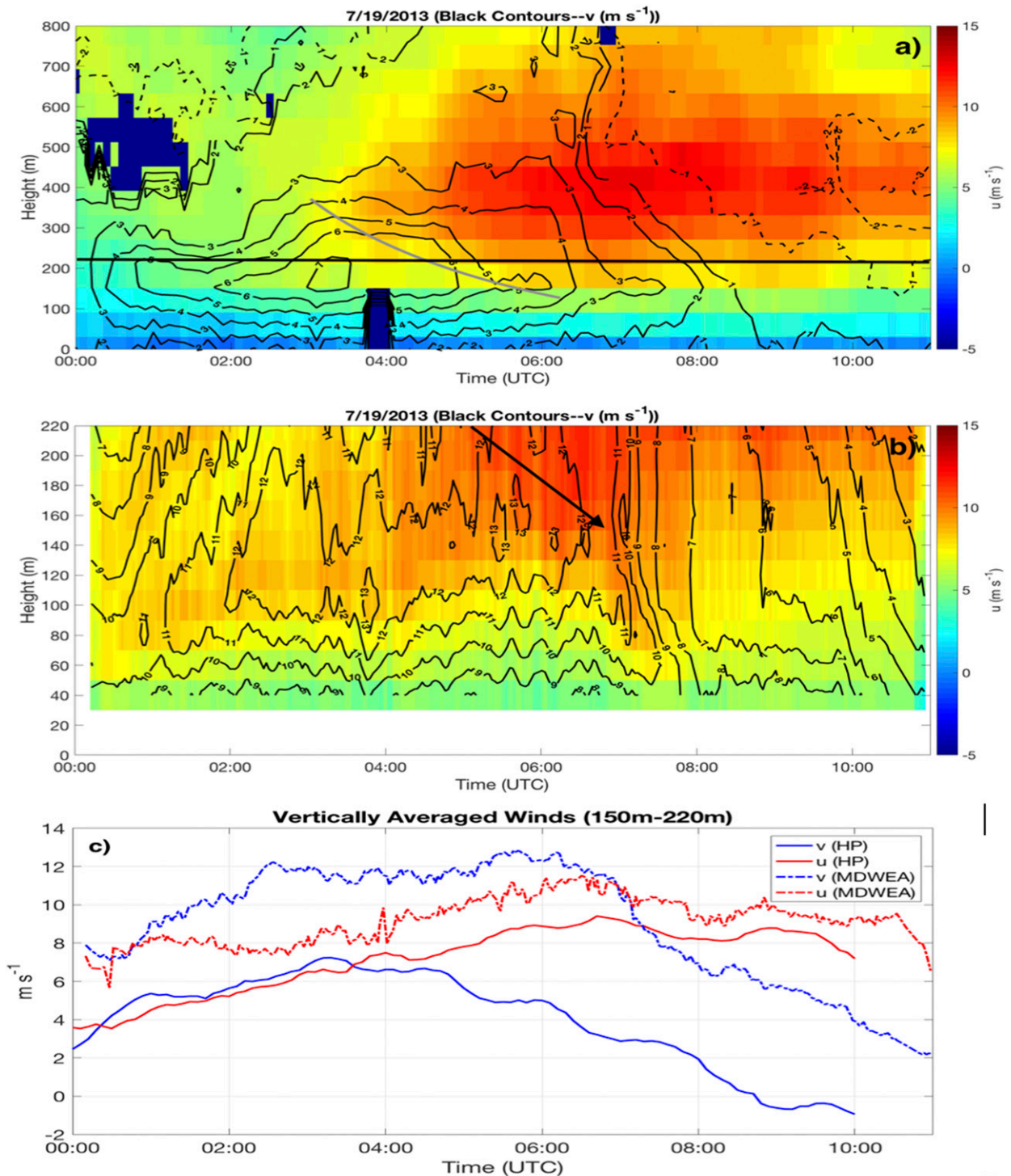


FIG. 5. A time evolution of profiles of v (black contours) and u (colors) for the (a) HP radar wind profiler and (b) Doppler wind lidar at MDWEA. The curved gray line in (a) represents the transition to a westerly dominated flow while the horizontal black line represents the upper limit of the lidar range. The black arrow in (b) represents the general progression of increased winds with respect to time aloft. (c) Vertically averaged component winds (v , blue; u , red) between 150 and 220 m are represented for both HP (solid) and MDWEA (dotted-dashed). The dark-blue area near 0400 UTC in (a) represents a period of no data collection for those heights.

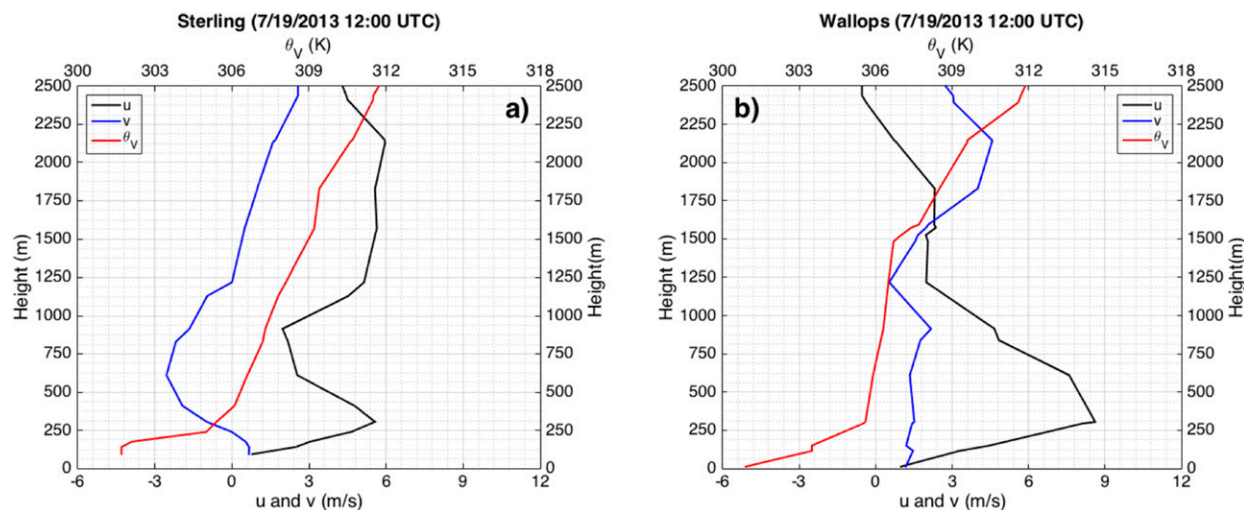


FIG. 6. Profiles of virtual potential temperature (red), v (blue), and u (black) for (a) Sterling and (b) Wallops Island at 1200 UTC 19 Jul 2013.

help explain the differences observed as the downslope wind interacted with LLJs in the mid-Atlantic region.

1) LARGE-SCALE AND SHALLOW BAROCLINIC FORCING

Two moderately strong LLJs (i.e., between 11 and 13 m s^{-1}) oriented from the south to southwest (Figs. 7c,d and 8a,b) were reproduced 200 m above the Chesapeake Bay and Atlantic Ocean by WRF, and coincide with regions of stable stratification (virtual potential temperature in Figs. 8a,b) near the surface and locally enhanced baroclinicity (i.e., steeper slope relative to the broader baroclinic trend in Fig. 8c). Delmarva, which coincides with a well-mixed region (Fig. 8a) in between the Chesapeake Bay and Atlantic Ocean early in the evening, locally reduced the overall baroclinicity by counteracting the broader baroclinicity; note the increased thickness shown by the green plotline (positive slope between third and fourth vertical dashed lines in Fig. 8c) and the decreased slope of the overall baroclinicity shown in blue over Delmarva in Fig. 8c. This prevented the formation of an LLJ over Delmarva early in the evening (see Fig. 8a) while supporting the formation of LLJs over both the Chesapeake Bay and Atlantic Ocean. The forcing of LLJs over the Chesapeake Bay and the Atlantic Ocean can be understood by the fact that the direction of regional forcing is in the same direction as the broader baroclinic forcing. Additional forcing is also present over the Chesapeake Bay as a result of winds traversing from rougher to smoother terrain, which is later discussed in section 4d(3). Together, this resulted in significant spatial variability of low-level winds east of the Appalachian Mountains

shown on the 1000-hPa pressure surface in Figs. 7c,d, with winds strongest over water bodies and along coastal regions.

Cooler SSTs along the Delmarva coast (i.e., cold tongue of near-surface virtual potential temperature along the Delmarva coast in Figs. 7a,b) and advection of a warm air layer from land due to adiabatically compressed air (recall the modified potential temperature profiles along the east–west transect from Fig. 4 with time) also impacted the baroclinicity. The region of cool SSTs observed along the coast indicates a possibility of coastal upwelling, while modifications to the thermal structure occurred as northwesterly flows moved across the mid-Atlantic region and into MDWEA. The former results if the synoptic-scale pressure distribution favors a substantial wind component along the coast that acts to displace water at the surface through wind stress (Bakun 1990). Since winds were persistent from the southwesterly direction, this likely promoted the cold pool coastal region observed along the MAB.

Later in the evening as the land surface cooled, a stable layer developed over Delmarva and regions west of the Chesapeake Bay (see virtual potential temperatures in Figs. 7b and 8b). This weakened the baroclinicity between land and sea through a decrease in the land–sea temperature difference and, furthermore, resulted in weaker cross-coastal horizontal wind gradients and a decrease in the coastal LLJ wind speed by nearly 3 m s^{-1} . Moreover, horizontal gradients in the wind across coastal boundaries (i.e., across the Chesapeake Bay and coastal ocean) also became less pronounced later in the evening, as evidenced in Fig. 7d.

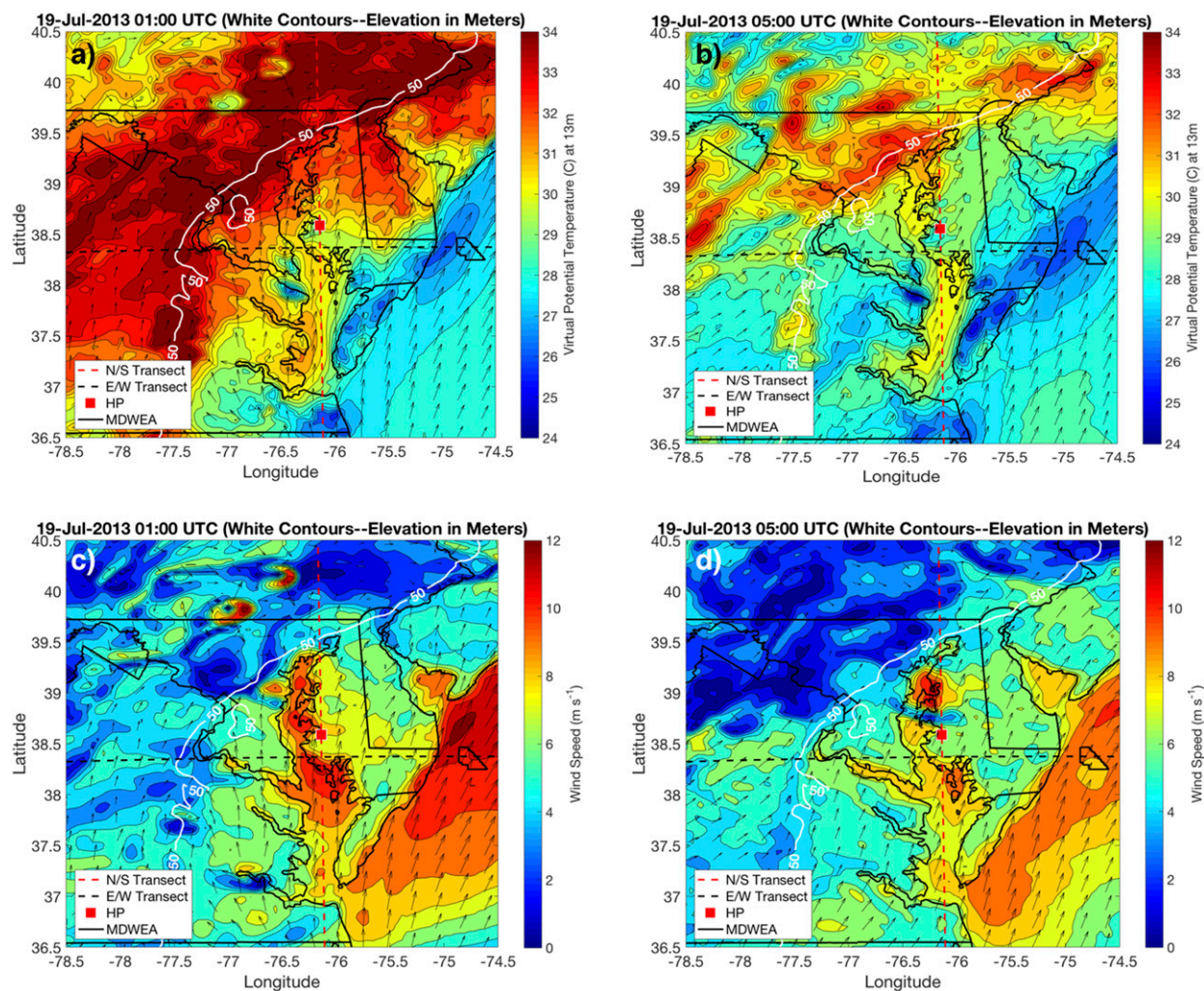


FIG. 7. A plan-view map of 13-m virtual potential temperature and wind vectors at 48 m at (a) 0100 and (b) 0500 UTC; and the 48-m wind speed with wind vectors at (c) 0100 and (d) 0500 UTC. Annotations of the north–south transect (vertical red dashed line) and east–west transect (horizontal black dashed line) are included in addition to the HP (red square) and MDWEA (black solid outline) sites.

One hypothesis is that this independent weakening of the coastal LLJ enabled the downslope wind to abruptly overtake the coastal LLJ during the interaction. Other less clear possibilities may be related to differences in stability and moisture content between interacting air masses that were substantially different than the onshore counterpart; this remains to be seen. A companion paper intends to investigate the smaller-scale interaction through a mean/wave/turbulence budget analysis to determine the physical mechanism that led to this so-called ramp-down event.

2) INERTIAL OSCILLATION

Hodographs are used to investigate whether an inertial oscillation was present near 200 m for both WRF (Figs. 9a,b) and observational (Figs. 9c,d) data at both

HP and MDWEA. Periods of stable stratification are noted in magenta in Figs. 9a and 9b (i.e., model) by considering the vertical gradients in potential temperature from WRF. The black (MDWEA) and red (HP) colors refer to times when the potential temperature profile was uniform (neutral) or decreased with height (unstable) in Figs. 9a and 9b. The fact that the magenta line concealed the black line in Fig. 9b (refer to legend for various plot lines and markers) indicates that conditions were stable for the entire time over MDWEA according to WRF. To understand how the data compared with a pure inertial oscillation, an ideal representation of the inertial cycle (dashed line), which uses a set of solutions [Eqs. (1) and (2)] derived from the Ekman model in Van de Wiel et al. (2010) as initialized from a chosen starting point

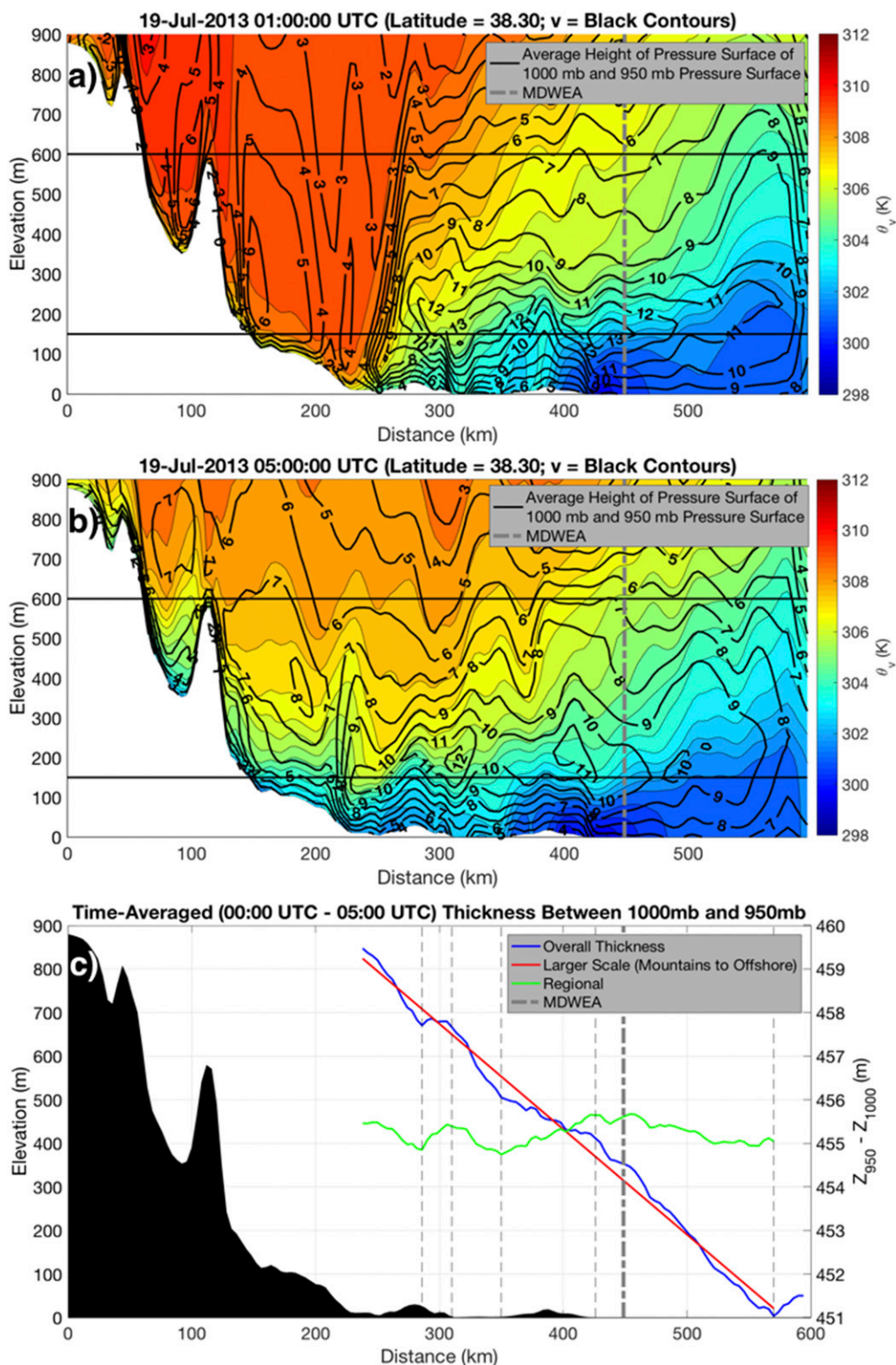


FIG. 8. The east–west cross section of profiles of virtual potential temperature (K, colors) overlaid with wind speed contours ($m s^{-1}$) at (a) 0100 and (b) 0500 UTC. (c) A time-averaged comparison (0000–0500 UTC) of the 1000–950-hPa thickness: overall (blue), larger scale (red), and regional (green). The MDWEA profile is highlighted in black. Average heights of pressure surfaces are indicated by black solid lines in (a) and (b), while the vertical gray dashed–dotted line indicates the approximate position of MDWEA. The smaller vertical dashed black lines represent topographical transitional points from west to east such as the fall line, the west end of the Chesapeake Bay, the west and east ends of Delmarva, and areas far offshore.

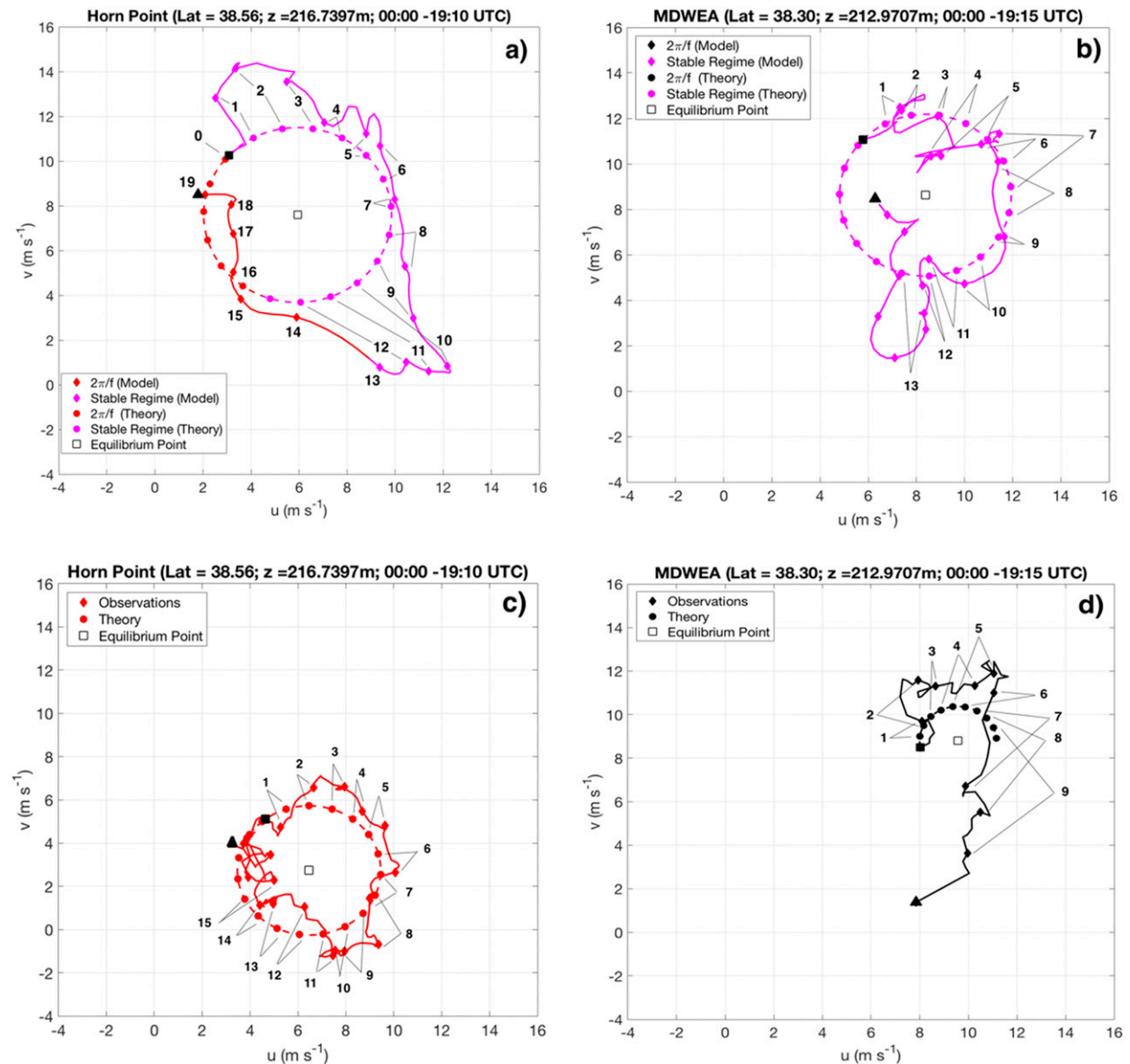


FIG. 9. Hodographs of (a) model at HP, (b) model at MDWEA, (c) observations at HP, and (d) observations at MDWEA. Magenta coloring in the model indicates times of stability, while the other colors indicate times of neutral to unstable conditions. Symbols are plotted hourly with numbers included to denote the hour associated with the symbol. A starting (square) and an ending (triangle) point are included in addition to the equilibrium point (white square).

$$u - u_{eq} = (v_0 - v_{eq}) \sin ft + (u_0 - u_{eq}) \cos ft \quad (1)$$

and

$$v - v_{eq} = (v_0 - v_{eq}) \cos ft + (u_0 - u_{eq}) \sin ft \quad (2)$$

(squares in Fig. 9) and closed by the end of a single period (triangles in Fig. 9) corresponding to the latitude of the site (~ 19.5 h), was overlaid with the output in each panel; note that v_0 and u_0 are the initial points (black

squares), v_{eq} and u_{eq} are the equilibrium points (white squares), and f is the Coriolis parameter. Symbols are included to mark the hourly progression of the inertial oscillation. For both WRF and the observations, the HP site provides clear evidence of Blackadar's inertial oscillation theory by showing a progression of rotation of the wind vector with respect to the equilibrium point centered on the white square, which should not be confused with the geostrophic wind vector since frictional effects are considered in this model, thus

resulting in a height dependence of the equilibrium wind throughout the extent of the boundary layer (Van de Wiel et al. 2010). This, however, was not observed in MDWEA for Figs. 9b and 9d, which show little to no agreement in how the wind vector rotates with time relative to the ideal case. This is likely due to the fact that the marine boundary layer does not change appreciably after sunset and baroclinic forcing along the coast was fairly strong, thus restricting the extent of wind vector rotation through preferential forcing linked to land–sea thermal gradients.

The HP hodograph shows overlying features protruding beyond the radius of the ideal inertial cycle, which is indicative of additional forcing (Shapiro and Fedorovich 2009). The first, which is located in the upper portions of Figs. 9a and 9c, occurs between 0100 and 0300 UTC, and the second, located at the bottom right of Figs. 9a and 9c occurs between 0800 and 1300 UTC. The first protrusion in Fig. 9a was found to be coincident in time and height (~ 200 m) with observations of the LLJ, thus indicating additional forcing of the LLJ. The second protrusion, on the other hand, occurred as the LLJ eroded and the eastward wind increased. The eastward winds (recall the transition to westerly dominated flows in Fig. 5a) revealed a strengthening in the eastward wind with time toward the surface, which is coincident in time and direction as forcing related to the downslope wind.

To account for the first protruding features in Figs. 9a and 9c, the average of the difference between Blackadar's ideal inertial oscillation theory with results from the observations and WRF can be used as a measure to crudely approximate additional LLJ forcing with respect to the equilibrium point (white square at the center). Difference calculations reveal contributions of additional forcing of 50% and 20% of Blackadar's inertial oscillation theory for WRF and observations, respectively. At HP, the early evolution is due to frictional decoupling and acceleration over the bay as a result of the long north–south fetch.

The hodographs for MDWEA are quite different between the model (Fig. 9b) and the observations (Fig. 9d) after 0500 UTC. In particular, observations show a rapid reduction in v with winds sustaining in u . This break in structure is linked to the rapid changes that occur as the downslope wind enters MDWEA. The model fails to show a break in the structure, but rather a gradual reduction in v with winds in u beginning to weaken after 0900 UTC.

Other factors that may have played a role in wind vector rotation were also considered, such as bay- and sea-breeze effects; however, through an analysis of surface stations along coastal regions (i.e., buoys in the Chesapeake Bay and near Ocean City) and WRF, it was

not clear that bay–sea-breeze effects were present during the case study. One possibility is that the bay- and sea-breeze effects were small relative to larger-scale southwesterly forcing or other sea-breeze types as described by Steele et al. (2013). In addition, as the day transitioned into night, and land–sea differences became smaller, the effects of bay and sea breezes would have been minimized, which would not have contributed to the rotation of winds as observed in Figs. 9a and 9c.

3) ADVECTION ACROSS A COASTAL TRANSITION

As shown earlier, the HP site coincided with a region of stronger winds over the Chesapeake Bay and was the result of baroclinic forcing; however, the situation appears to be a bit more complex since winds toward the north end of the Chesapeake Bay are comparable to MDWEA (only 2 m s^{-1} or less) despite having a much weaker shallow baroclinic signature; recall the difference in the cross-coastal virtual potential temperature structure across the land–sea boundary for both the Chesapeake Bay and MDWEA in Fig. 7a. One possible explanation for the stronger winds over the bay, especially farther north near HP, is that acceleration of winds over the Chesapeake Bay occurred after sunset. The increase in winds with fetch distance across the bay is depicted along the red dashed line in Fig. 7. Figures 10a and 10b assess changes in the northward wind (black contours) along the red dashed line that intersects HP in Fig. 7. It is observed from WRF at 0100 UTC that winds increase substantially by 4 m s^{-1} after crossing from Virginia into the Chesapeake Bay (note the gray arrow showing the land–sea boundary at the bottom of Fig. 10) a distance of 100 km downstream (i.e., from 50 to 150 km). Winds begin to weaken upon transitioning back onto shore in Maryland at 200 km, where a wave-like disturbance in both v and potential temperature is observed near the coastal transition from the south—a feature commonly produced in the presence of topographic variability or terrain discontinuities (Nappo 2013). This is likely due to gravity waves generated by a geostrophic adjustment after sunset when land–sea temperature gradients are changing rapidly. The strength of the winds, however, is not diminished completely, thus indicating that the increase in wind from rough to smooth terrain (Barthelmie et al. 2007) was partially retained and had a lasting impact between 0100 and 0400 UTC as shown in the HP hodographs.

To further reveal the impacts of winds crossing into the Chesapeake Bay from Virginia, an analysis of the horizontal equation of motion for the north-pointing wind was conducted using WRF model data, where the dominant terms along the red-dashed transect were found to be the advection and diffusion terms. The

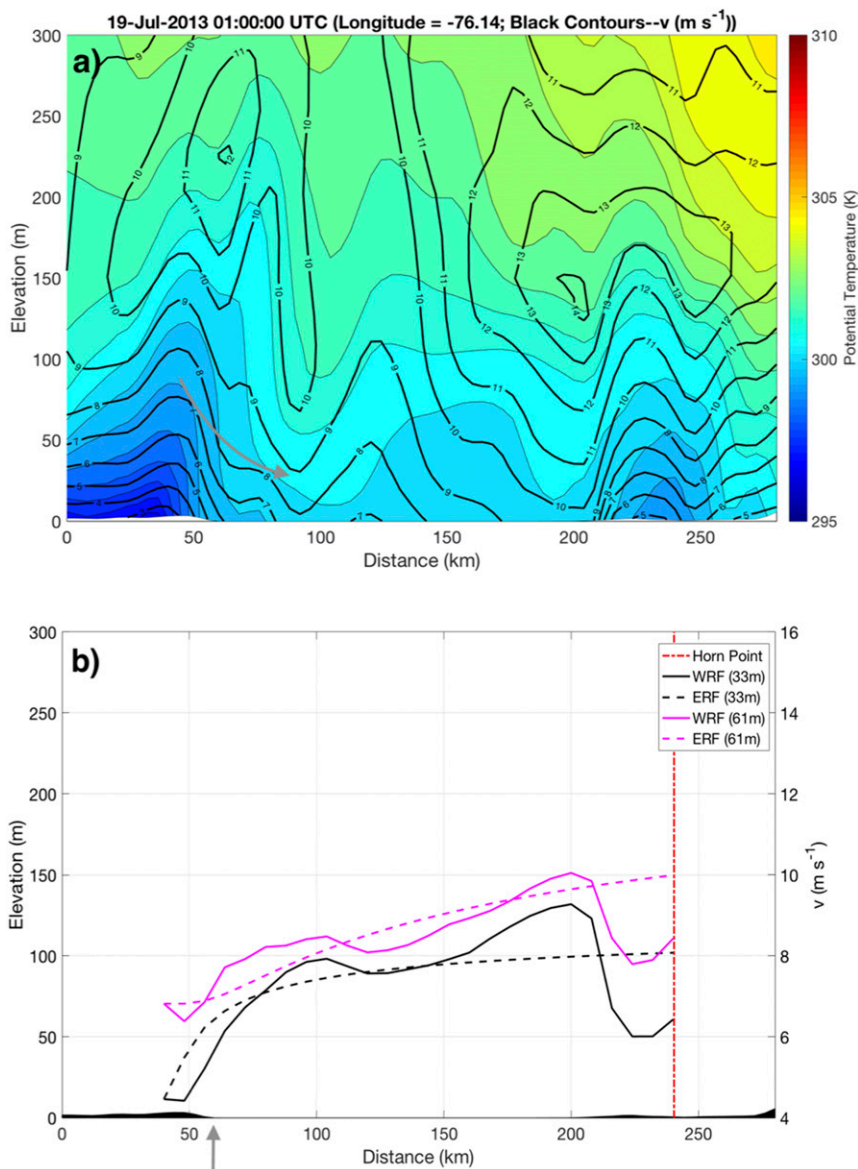


FIG. 10. (a) Profiles of v (black contours) and potential temperature (colors), and (b) v from WRF (solid) and v derived using the error function (ERF) solution to the advection–diffusion equation (dashed) at 33 m (white) and 61 m (magenta) along the north–south transect shown in Fig. 7. The vertical red dashed–dotted line denotes the HP location along the north–south transect. Gray arrow in (a) shows downward momentum toward the surface across the coastal transition between Virginia and Chesapeake Bay while the gray arrow below (b) shows the location of the coastal boundary.

solution to the advection–diffusion equation, which was applied for all heights, satisfies a reduced form of the Navier–Stokes equation since 1) the local changes in wind with time were relatively small in comparison with advection ($\partial v/\partial t \sim 0.3v\partial v/\partial y$ overall, and $\partial v/\partial t \sim 0.2v\partial v/\partial y$ as the wind transitioned across the coast), 2) the change in winds traversing the coastal boundary resulted in a relatively large friction term in comparison with the background pressure gradient (i.e., generally weak synoptic

pressure gradient extending across the mid-Atlantic region), and 3) the westerly component was both relatively small and its time scale was less than 3 h, thus rendering the Coriolis term negligible. The physical reasoning behind the advection–diffusion equation is that it relates to a change in the low-level forcing of the near-surface wind as a result of winds moving from a rough surface to a smooth surface, thus contributing to an increase in momentum flux convergence across the

boundary (Garratt 1990). The eddy diffusivity inside the frictional term (i.e., $K\partial^2v/\partial z^2$) was determined by analyzing WRF Model wind profiles exhibiting Ekman profile behavior, applying both surface and geostrophic boundary conditions for each case, and fitting the Ekman behavior to extract eddy diffusivity. A spatio-temporal average of the eddy diffusivity was performed for all profiles exhibiting Ekman-like characteristics, with a value of $0.18\text{ m}^2\text{ s}^{-1}$. Further modifications to find the best fit between WRF and winds using the solution to the advection diffusion equation were then applied by considering a height dependence on the eddy diffusivity in the form of a power law such that the eddy diffusivity decreased with height (i.e., less friction at higher heights) (Garratt 1990).

Comparisons between the north-pointing wind from WRF (solid plot lines) across the red transect from Fig. 7 and a derivation of the north-pointing wind using the solution to the advection–diffusion equation (dashed lines) for 33 m (white) and 61 m (magenta) from Fig. 10b reveal strong agreement. It is clear that the overall behavior is preserved by this solution as winds traverse the coastal boundary, that the winds strengthened upon crossing the coast, and that the Chesapeake Bay provided a long enough fetch where winds began to level off after traveling nearly 100 km northward from the mouth of the bay. It is important to note that the difference in the northward wind between the initial value (i.e., near coastal discontinuity) and HP site is approximately 2 m s^{-1} , which is similar to the averaged difference observed in Fig. 9a between WRF and the inertial oscillation solutions between the 0100 and 0400 UTC time periods. One should be careful when inferring an exact relationship between the difference in the inertial oscillation solution and the increase in winds with fetch, however, since the impacts of the Chesapeake Bay on winds were evaluated well below 200 m.

Another feature in Fig. 10a that appears to be important to wind forcing from Virginia into the Chesapeake Bay is the change in cross-coastal stability near the gray arrow at the bottom of Fig. 10. As can be seen, stronger winds from aloft descended toward the surface nearly along the isentropes. It is hypothesized that the cross-coastal baroclinic zone contributed to winds accelerating into the bay, which is both different and independent of the increase in winds observed at the north end of the bay. According to Fig. 10a, the acceleration of winds across the coast was the result of differences in stability, which impacted the wind profile within the first 100 m of the atmosphere, whereas winds show a more uniform increase across the first 300 m with increasing fetch from the midpoint of the bay onward.

5. Discussion and conclusions

The primary goals of this study have been to illustrate 1) the importance of both large-scale and regional forcing on the on- and offshore wind profiles, 2) the impact of topographical forcing from terrain farther inland on the offshore wind, and 3) different responses in the wind profile as the downslope wind moved across the mid-Atlantic region. Two large-scale patterns (BH and L) impacted the region and provided ideal background conditions for both LLJs and the downslope wind. Southwesterly flows from BH reinforced LLJs over the coastal plain and along the Delmarva coast. Moreover, cooler waters along the coast, which served as a primary forcing component of the coastal LLJ in setting up a cross-coastal thermal gradient, were likely caused by enhanced wind stress near the surface from persistent southwesterly winds (Schofield et al. 2008). The shift to westerly flows during the evening was the result of the eastward movement of L, the north–south alignment of L with H, and the tightening of the pressure gradient that enhanced winds as they rotated from a southwesterly-to-westerly flow. This promoted substantial cross-mountain flows that deepened the lee trough and triggered a downslope wind. It is hypothesized that the combination of BH and an eastward-moving low provided the unique conditions responsible for the LLJ–downslope wind interaction. A future study aims to evaluate the statistical significance of these features and the likelihood that both an LLJ and a downslope wind are observed.

Considerable work has been done to evaluate the impact of topography on the wind profile in the mid-Atlantic region, but little has been done to evaluate whether topographical forcing, from either the Appalachian Mountains or other land features, can significantly impact winds along the coast offshore. The evaluation of inland sources on the offshore wind profile was made possible through interrogating data gathered during the MDWEA campaign. Combined observations from both a nearby sounding (Wallops Island) and the Doppler lidar revealed a westerly wind maximum and a shift to westerly flows comparable to that observed farther inland at Cambridge. This study is novel in that it provides strong evidence of downslope flows from the Appalachian Mountains moving offshore and resulting in significant dynamical changes within a short period of time. Moreover, this work incentivizes future studies of marine boundary layer winds along the coast due to the inherent complexity of winds in this region caused by on- and offshore forcing and the evolving background conditions.

The evaluation of WRF Model runs for this study was imperative for identifying key differences between on- and offshore sites that could not be performed by analyzing observations alone. WRF revealed two LLJs, one over the coastal plain and the other along the Delmarva coast, forced by a combination of various forcing mechanisms linked to the topography. Forcing mechanisms of the LLJ over the coastal plain were consistent with baroclinic forcing between the Chesapeake Bay and Delmarva, radiative cooling over the land and the decoupling of winds from the surface, and an acceleration of flow traversing from Virginia into the Chesapeake Bay as a result of changes in both roughness and stability. The coastal LLJ, on the other hand, was forced strictly by baroclinic forcing, which as revealed by WRF was significantly stronger than the baroclinic forcing between Delmarva and the Chesapeake Bay. Another major difference between the LLJ over the coastal plain and the coastal LLJ was the fact that the coastal LLJ noticeably weakened during the early morning hours as surface temperatures over land cooled to values comparable to the sea surface. This lessened the baroclinic forcing and may be one of the major contributing factors to the different responses in the wind profiles observed between sites, namely, the simultaneous weakening of the coastal LLJ as the downslope wind propagated into MDWEA. A future study is planned to evaluate the small-scale response from the point of view of boundary layer dynamics by considering the mean/wave/turbulent components of the flow during the interaction between the coastal LLJ and downslope wind.

Because of a lack of observations, very little is known about the detailed mechanisms that force the winds in the marine boundary layer in near-coastal areas of the mid-Atlantic where offshore wind development is being considered. The observations from the 2013 summer offshore campaign were somewhat surprising in that they were more variable than expected, with diurnal signatures that suggested influences from the land. This led to an investigation of mechanisms by which the inland and coastal terrain could impact winds offshore. While this study was limited to the warm season, primarily because data were available for that time period, the wind regimes offshore during the warm season could perhaps be influenced to a greater degree by the coastal and inland terrain during periods of weak synoptic forcing. The warm season is also important because the electrical load is higher during that time of year. It is also important to study the warm season in more detail since statistically higher occurrence rates of highly sheared flows are more frequent than in the cold season despite weaker synoptic conditions (Ryan 2004; Zhang et al. 2006).

Acknowledgments. The authors are grateful to the Maryland Energy Administration for support of this work and also thank Dr. Julio Bacmeister for many helpful discussions.

REFERENCES

- Archer, C. L., and Coauthors, 2014: Meteorology for coastal/offshore wind energy in the United States: Recommendations and research needs for the next 10 years. *Bull. Amer. Meteor. Soc.*, **95**, 515–519, <https://doi.org/10.1175/BAMS-D-13-00108.1>.
- Baker, R. D., B. H. Lynn, A. Boone, W.-K. Tao, and J. Simpson, 2001: The influence of soil moisture, coastline curvature, and land-breeze circulations on sea-breeze-initiated precipitation. *J. Hydrometeorol.*, **2**, 193–211, [https://doi.org/10.1175/1525-7541\(2001\)002<0193:TIOSMC>2.0.CO;2](https://doi.org/10.1175/1525-7541(2001)002<0193:TIOSMC>2.0.CO;2).
- Bakun, A., 1990: Global climate change and intensification of coastal ocean upwelling. *Science*, **247**, 198–201, <https://doi.org/10.1126/science.247.4939.198>.
- Banta, R. M., 2008: Stable-boundary-layer regimes from the perspective of the low-level jet. *Acta Geophys.*, **56**, 58–87, <https://doi.org/10.2478/s11600-007-0049-8>.
- , and P. T. Gannon Jr., 1995: Influence of soil moisture on simulations of katabatic flow. *Theor. Appl. Climatol.*, **52**, 85–94, <https://doi.org/10.1007/BF00865509>.
- , Y. L. Pichugina, and W. A. Brewer, 2006: Turbulent velocity-variance profiles in the stable boundary layer generated by a nocturnal low-level jet. *J. Atmos. Sci.*, **63**, 2700–2719, <https://doi.org/10.1175/JAS3776.1>.
- Barthelmie, R., J. Badger, S. Pryor, C. B. Hasager, M. B. Christiansen, and B. Jørgensen, 2007: Offshore coastal wind speed gradients: Issues for the design and development of large offshore windfarms. *Wind Eng.*, **31**, 369–382, <https://doi.org/10.1260/030952407784079762>.
- Beaudry-Losique, J., and Coauthors, 2011: A national offshore wind strategy: Creating an offshore wind energy industry in the United States. Office of Energy Efficiency and Renewable Energy Tech. Rep., 42 pp., https://energy.gov/sites/prod/files/2013/12/t5/national_offshore_wind_strategy.pdf.
- Bell, G. D., and L. F. Bosart, 1988: Appalachian cold-air damming. *Mon. Wea. Rev.*, **116**, 137–161, [https://doi.org/10.1175/1520-0493\(1988\)116<0137:ACAD>2.0.CO;2](https://doi.org/10.1175/1520-0493(1988)116<0137:ACAD>2.0.CO;2).
- Blackadar, A. K., 1957: Boundary layer wind maxima and their significance for the growth of nocturnal inversions. *Bull. Amer. Meteor. Soc.*, **38**, 283–290.
- Bonner, W. D., 1968: Climatology of the low level jet. *Mon. Wea. Rev.*, **96**, 833–850, [https://doi.org/10.1175/1520-0493\(1968\)096<0833:COTLLJ>2.0.CO;2](https://doi.org/10.1175/1520-0493(1968)096<0833:COTLLJ>2.0.CO;2).
- Burk, S. D., and W. T. Thompson, 1996: The summertime low-level jet and marine boundary layer structure along the California coast. *Mon. Wea. Rev.*, **124**, 668–686, [https://doi.org/10.1175/1520-0493\(1996\)124<0668:TSLLJA>2.0.CO;2](https://doi.org/10.1175/1520-0493(1996)124<0668:TSLLJA>2.0.CO;2).
- Chen, F., and J. Dudhia, 2001: Coupling an advanced land surface–hydrology model with the Penn State–NCAR MM5 modeling system. Part I: Model implementation and sensitivity. *Mon. Wea. Rev.*, **129**, 569–585, [https://doi.org/10.1175/1520-0493\(2001\)129<0569:CAALSH>2.0.CO;2](https://doi.org/10.1175/1520-0493(2001)129<0569:CAALSH>2.0.CO;2).
- Colle, B. A., and D. R. Novak, 2010: The New York Bight jet: Climatology and dynamical evolution. *Mon. Wea. Rev.*, **138**, 2385–2404, <https://doi.org/10.1175/2009MWR3231.1>.
- , M. J. Sienkiewicz, C. Archer, D. Veron, F. Veron, W. Kempton, and J. E. Mak, 2016: Improving the Mapping and

- Prediction of Offshore Wind Resources (IMPOWR): Experimental overview and first results. *Bull. Amer. Meteor. Soc.*, **97**, 1377–1390, <https://doi.org/10.1175/BAMS-D-14-00253.1>.
- Crook, N. A., 1988: Trapping of low-level internal gravity waves. *J. Atmos. Sci.*, **45**, 1533–1541, [https://doi.org/10.1175/1520-0469\(1988\)045<1533:TOLLIG>2.0.CO;2](https://doi.org/10.1175/1520-0469(1988)045<1533:TOLLIG>2.0.CO;2).
- Cuxart, J., and Coauthors, 2000: Stable Atmospheric Boundary-Layer Experiment in Spain (SABLES 98): A report. *Bound.-Layer Meteor.*, **96**, 337–370, <https://doi.org/10.1023/A:1002609509707>.
- Decker, S. G., and D. A. Robinson, 2011: Unexpected high winds in northern New Jersey: A downslope windstorm in modest topography. *Wea. Forecasting*, **26**, 902–921, <https://doi.org/10.1175/WAF-D-10-05052.1>.
- Doyle, J. D., and T. T. Warner, 1993: A three-dimensional numerical investigation of a Carolina coastal low-level jet during GALE IOP 2. *Mon. Wea. Rev.*, **121**, 1030–1047, [https://doi.org/10.1175/1520-0493\(1993\)121<1030:ATDNIO>2.0.CO;2](https://doi.org/10.1175/1520-0493(1993)121<1030:ATDNIO>2.0.CO;2).
- Durran, D. R., 2003: Downslope winds. *Encyclopedia of Atmospheric Sciences*, J. Holton and J. Curry, Eds., Elsevier, 644–650.
- Gaffin, D. M., 2002: Unexpected warming induced by foehn winds in the lee of the Smoky Mountains. *Wea. Forecasting*, **17**, 907–915, [https://doi.org/10.1175/1520-0434\(2002\)017<0907:UWIBFW>2.0.CO;2](https://doi.org/10.1175/1520-0434(2002)017<0907:UWIBFW>2.0.CO;2).
- Garratt, J., 1990: The internal boundary layer: A review. *Bound.-Layer Meteor.*, **50**, 171–203, <https://doi.org/10.1007/BF00120524>.
- Grachev, A. A., L. S. Leo, S. Di Sabatino, H. J. Fernando, E. R. Pardyjak, and C. W. Fairall, 2016: Structure of turbulence in katabatic flows below and above the wind-speed maximum. *Bound.-Layer Meteor.*, **159**, 469–494, <https://doi.org/10.1007/s10546-015-0034-8>.
- Haiden, T., and C. D. Whiteman, 2005: Katabatic flow mechanisms on a low-angle slope. *J. Appl. Meteor.*, **44**, 113–126, <https://doi.org/10.1175/JAM-2182.1>.
- Holt, T. R., 1996: Mesoscale forcing of a boundary layer jet along the California coast. *J. Geophys. Res.*, **101**, 4235–4254, <https://doi.org/10.1029/95JD03231>.
- Holton, J. R., 1967: The diurnal boundary layer wind oscillation above sloping terrain. *Tellus*, **19**, 200–205, <https://doi.org/10.3402/tellusa.v19i2.9766>.
- Houze, R. A., Jr., 2012: Orographic effects on precipitating clouds. *Rev. Geophys.*, **50**, <https://doi.org/10.1029/2011RG000365>.
- Huang, H.-L., C.-C. Wang, G. T.-J. Chen, and R. E. Carbone, 2010: The role of diurnal solenoidal circulation on propagating rainfall episodes near the eastern Tibetan Plateau. *Mon. Wea. Rev.*, **138**, 2975–2989, <https://doi.org/10.1175/2010MWR3225.1>.
- Iacono, M., E. Mlawer, S. Clough, and J. Morcrette, 1998: Effects of a validated longwave radiation model, RRTM, on GCM simulations. *Eighth Atmospheric Radiation Measurement (ARM) Science Team Meeting*, Tucson, AZ, Atmospheric Radiation Measurement (ARM) Climate Research Facility.
- Janjić, Z. I., 1994: The step-mountain eta coordinate model: Further developments of the convection, viscous sublayer, and turbulence closure schemes. *Mon. Wea. Rev.*, **122**, 927–945, [https://doi.org/10.1175/1520-0493\(1994\)122<0927:TSMECM>2.0.CO;2](https://doi.org/10.1175/1520-0493(1994)122<0927:TSMECM>2.0.CO;2).
- Mahrt, L., 1998: Nocturnal boundary-layer regimes. *Bound.-Layer Meteor.*, **88**, 255–278, <https://doi.org/10.1023/A:1001171313493>.
- , D. Vickers, and E. L. Andreas, 2014: Low-level wind maxima and structure of the stably stratified boundary layer in the coastal zone. *J. Appl. Meteor. Climatol.*, **53**, 363–376, <https://doi.org/10.1175/JAMC-D-13-0170.1>.
- Mercer, A. E., M. B. Richman, H. B. Bluestein, and J. M. Brown, 2008: Statistical modeling of downslope windstorms in Boulder, Colorado. *Wea. Forecasting*, **23**, 1176–1194, <https://doi.org/10.1175/2008WAF2007067.1>.
- Meyers, M. P., J. S. Snook, D. A. Wesley, and G. S. Poulos, 2003: A Rocky Mountain storm. Part II: The forest blowdown over the west slope of the northern Colorado mountains: Observations, analysis, and modeling. *Wea. Forecasting*, **18**, 662–674, [https://doi.org/10.1175/1520-0434\(2003\)018<0662:ARMSPI>2.0.CO;2](https://doi.org/10.1175/1520-0434(2003)018<0662:ARMSPI>2.0.CO;2).
- Monti, P., H. Fernando, M. Princevac, W. Chan, T. Kowalewski, and E. R. Pardyjak, 2002: Observations of flow and turbulence in the nocturnal boundary layer over a slope. *J. Atmos. Sci.*, **59**, 2513–2534, [https://doi.org/10.1175/1520-0469\(2002\)059<2513:OOFATI>2.0.CO;2](https://doi.org/10.1175/1520-0469(2002)059<2513:OOFATI>2.0.CO;2).
- Muñoz, E., A. J. Busalacchi, S. Nigam, and A. Ruiz-Barradas, 2008: Winter and summer structure of the Caribbean low-level jet. *J. Climate*, **21**, 1260–1276, <https://doi.org/10.1175/2007JCLI1855.1>.
- Nappo, C. J., 2013: *An Introduction to Atmospheric Gravity Waves*. International Geophysics Series, Vol. 102, Academic Press, 400 pp.
- Nunalee, C. G., and S. Basu, 2014: Mesoscale modeling of coastal low-level jets: Implications for offshore wind resource estimation. *Wind Energy*, **17**, 1199–1216, <https://doi.org/10.1002/we.1628>.
- Peng, M. S., S.-W. Li, S. W. Chang, and R. Williams, 1995: Flow over mountains: Coriolis force, transient troughs and three dimensionality. *Quart. J. Roy. Meteor. Soc.*, **121**, 593–613, <https://doi.org/10.1002/qj.49712152307>.
- Poulos, G. S., and Coauthors, 2002: CASES-99: A comprehensive investigation of the stable nocturnal boundary layer. *Bull. Amer. Meteor. Soc.*, **83**, 555–581, [https://doi.org/10.1175/1520-0477\(2002\)083<0555:CACIOT>2.3.CO;2](https://doi.org/10.1175/1520-0477(2002)083<0555:CACIOT>2.3.CO;2).
- Rabenhorst, S., D. Whiteman, D.-L. Zhang, and B. Demoz, 2014: A case study of mid-Atlantic nocturnal boundary layer events during WAVES 2006. *J. Appl. Meteor. Climatol.*, **53**, 2627–2648, <https://doi.org/10.1175/JAMC-D-13-0350.1>.
- Ralph, F. M., P. J. Neiman, and D. Levinson, 1997: Lidar observations of a breaking mountain wave associated with extreme turbulence. *Geophys. Res. Lett.*, **24**, 663–666, <https://doi.org/10.1029/97GL00349>.
- Reinecke, P. A., and D. R. Durran, 2008: Estimating topographic blocking using a Froude number when the static stability is nonuniform. *J. Atmos. Sci.*, **65**, 1035–1048, <https://doi.org/10.1175/2007JAS2100.1>.
- Ryan, W. F., 2004: The low level jet in Maryland: Profiler observations and preliminary climatology. Rep. prepared for Maryland Department of the Environment, Air and Radiation Administration, 43 pp., http://www.mde.state.md.us/programs/Air/AirQualityPlanning/Documents/www.mde.state.md.us/assets/document/AirQuality/BALT_OZONE_SIP/Appendix_G5.pdf.
- Schofield, O., and Coauthors, 2008: The decadal view of the mid-Atlantic Bight from the COOLroom: Is our coastal system changing? *Oceanography*, **21**, 108–117, <https://doi.org/10.5670/oceanog.2008.08>.
- Schultz, D. M., 2005: A review of cold fronts with prefrontal troughs and wind shifts. *Mon. Wea. Rev.*, **133**, 2449–2472, <https://doi.org/10.1175/MWR2987.1>.
- , and R. J. Trapp, 2003: Nonclassical cold-frontal structure caused by dry subcloud air in northern Utah during the

- Intermountain Precipitation Experiment (IPEX). *Mon. Wea. Rev.*, **131**, 2222–2246, [https://doi.org/10.1175/1520-0493\(2003\)131<2222:NCSCBD>2.0.CO;2](https://doi.org/10.1175/1520-0493(2003)131<2222:NCSCBD>2.0.CO;2).
- Seluchi, M. E., F. A. Norte, P. Satyamurty, and S. C. Chou, 2003: Analysis of three situations of the foehn effect over the Andes (zonda wind) using the Eta–CPTEC regional model. *Wea. Forecasting*, **18**, 481–501, [https://doi.org/10.1175/1520-0434\(2003\)18<481:AOTSOT>2.0.CO;2](https://doi.org/10.1175/1520-0434(2003)18<481:AOTSOT>2.0.CO;2).
- Shapiro, A., and E. Fedorovich, 2009: Nocturnal low-level jet over a shallow slope. *Acta Geophys.*, **57**, 950–980.
- , —, and S. Rahimi, 2016: A unified theory for the Great Plains nocturnal low-level jet. *J. Atmos. Sci.*, **73**, 3037–3057, <https://doi.org/10.1175/JAS-D-15-0307.1>.
- Skamarock, W. C., and J. B. Klemp, 2008: A time-split non-hydrostatic atmospheric model for weather research and forecasting applications. *J. Comput. Phys.*, **227**, 3465–3485, <https://doi.org/10.1016/j.jcp.2007.01.037>.
- Smith, R. B., 1976: The generation of lee waves by the Blue Ridge. *J. Atmos. Sci.*, **33**, 507–519, [https://doi.org/10.1175/1520-0469\(1976\)033<0507:TGOLWB>2.0.CO;2](https://doi.org/10.1175/1520-0469(1976)033<0507:TGOLWB>2.0.CO;2).
- Sparling, L., S. Rabenhorst, B. William, R. Delgado, E. Strobach, B. Boicourt, and B. Bailey, 2013: Building a science-based foundation for assessing the offshore wind resource of Maryland. *Proc. EWEA Offshore*, Frankfurt, Germany, European Wind Energy Association.
- Steele, C., S. Dorling, R. Von Glasow, and J. Bacon, 2013: Idealized WRF Model sensitivity simulations of sea breeze types and their effects on offshore windfields. *Atmos. Chem. Phys.*, **13**, 443–461, <https://doi.org/10.5194/acp-13-443-2013>.
- Thompson, D. B., 2012: Appalachian lee troughs and their association with severe convective storms. M.S. thesis, Dept. of Atmospheric and Environmental Science, University at Albany, State University of New York, 137 pp., http://cstar.cestm.albany.edu/CAP_Projects/Thompson/thompson_thesis_total_16Aug.pdf.
- Van de Wiel, B. J., A. Moene, G. Steeneveld, P. Baas, F. Bosveld, and A. Holtslag, 2010: A conceptual view on inertial oscillations and nocturnal low-level jets. *J. Atmos. Sci.*, **67**, 2679–2689, <https://doi.org/10.1175/2010JAS3289.1>.
- Whiteman, C. D., and J. C. Doran, 1993: The relationship between overlying synoptic-scale flows and winds within a valley. *J. Appl. Meteor.*, **32**, 1669–1682, [https://doi.org/10.1175/1520-0450\(1993\)032<1669:TRBOSS>2.0.CO;2](https://doi.org/10.1175/1520-0450(1993)032<1669:TRBOSS>2.0.CO;2).
- , and S. Zhong, 2008: Downslope flows on a low-angle slope and their interactions with valley inversions. Part I: Observations. *J. Appl. Meteor. Climatol.*, **47**, 2023–2038, <https://doi.org/10.1175/2007JAMC1669.1>.
- , X. Bian, and S. Zhong, 1997: Low-level jet climatology from enhanced rawinsonde observations at a site in the southern Great Plains. *J. Appl. Meteor.*, **36**, 1363–1376, [https://doi.org/10.1175/1520-0450\(1997\)036<1363:LLJCFE>2.0.CO;2](https://doi.org/10.1175/1520-0450(1997)036<1363:LLJCFE>2.0.CO;2).
- Zardi, D., and C. D. Whiteman, 2013: Diurnal mountain wind systems. *Mountain Weather Research and Forecasting*, F. Chow et al., Eds., Springer, 35–119.
- Zhang, D.-L., S. Zhang, and S. J. Weaver, 2006: Low-level jets over the mid-Atlantic states: Warm-season climatology and a case study. *J. Appl. Meteor. Climatol.*, **45**, 194–209, <https://doi.org/10.1175/JAM2313.1>.